



19 **Abstract**

20 Tropical cyclones (TCs) with a high Saffir-Simpson scale can cause catastrophic damages
21 to coastal regions after landfall. Recent studies have linked the TC's devastation to climate change
22 that induces favorable environmental conditions, such as increasing sea-surface temperature, to
23 supercharge the storms. Also, atmospheric aerosols likely impact the development and intensity of
24 TCs, but their effects remain poorly understood, particularly coupled with the ocean dynamics.
25 Here we quantitatively assess the aerosol microphysical effects and aerosol-modified ocean
26 feedbacks during Hurricane Katrina using a cloud-resolving atmosphere-ocean coupled model -
27 Weather Research and Forecasting (WRF) in conjunction with the Regional Ocean Model System
28 (ROMS). Our model simulations reveal that an enhanced destructive power of the storm, as
29 reflected by larger integrated kinetic energy, heavier precipitation, and higher sea-level rise, is
30 linked to the combined effects of aerosols and ocean feedbacks. These effects further result in an
31 expansion of the storm circulation with a reduced intensity because of decreasing moist static
32 energy supply and enhancing vorticity Rossby wave outward propagation. Both accumulated
33 precipitation and storm surge are enhanced during the mature stage with elevated aerosol
34 concentrations, implying exacerbated flooding damage over the coastal region. The ocean
35 feedback following the aerosol microphysical effects tends to mitigate the Ekman upwelling
36 cooling and offsets the aerosol-induced storm weakening, by invigorating cloud and precipitation
37 near the eyewall region. Our results highlight the importance of accounting for the effects of
38 aerosol microphysics and ocean-coupling feedbacks to improve the forecast of TC destructiveness,
39 particularly near the heavily polluted coastal regions along the Gulf of Mexico.

40



41 **1. Introduction**

42 The destruction of Hurricane Katrina that struck New Orleans, Louisiana in late August
43 2005 was measured by the maximum wind speed at landfall and the hundreds of kilometers of the
44 coast areas affected by severe storm surge of more than 3 m. Hurricane Katrina progressed inland
45 as a category 3 storm (with sustained winds of 194 km hour⁻¹) and generated significant storm
46 surge exceeding 10 m on the Mississippi coast and up to 6 m southeast of New Orleans, with up
47 to 2 m of additional wave run-up in the most exposed location (Fritz et al., 2007; NWS, 2016).
48 The catastrophic damage associated with hurricanes in recent decades is exemplified as the
49 evidence of increasing devastation of tropical cyclones (TCs) relevant to changing climate
50 (Emanuel, 2005, 2017; Knutson et al., 2019; van Oldenborgh et al., 2017), which induces favorable
51 environmental conditions (such as increasing SST) to supercharge hurricanes and increasing the
52 risk of major damage (Trenberth et al., 2018). Another key feature of TC lies in the efficient
53 formation of hydrometeors and large latent heat release that fuels the TC development and
54 destruction via strong winds, heavy precipitation, storm surge, and flooding (Pan et al., 2020).
55 Currently, the effects of the abovementioned factors on the destructive power of TCs remain to be
56 quantified and isolated.

57 There now exist compelling evidence that natural and anthropogenic aerosols play critical
58 roles in the genesis and development of TCs (Khain et al., 2010; Herbener et al., 2014; Khain et
59 al., 2016; Pan et al., 2018; Rosenfeld et al., 2012; Wang et al., 2014). By acting as cloud
60 condensation nuclei (CCN), aerosol particles can lower the requirement of supersaturated
61 condition for cloud formation (Fan et al., 2018; Wang et al., 2011). A previous modeling study
62 demonstrated that high aerosol levels invigorate rainbands and increase precipitation, but decrease
63 the eyewall strength (Zhang et al., 2009; Khain et al., 2010; Rosenfeld et al., 2012; Wang et al.,



64 2014). Particularly for Hurricane Katrina, Khain et al. (2008; 2010) and Wang et al. (2014) found
65 that aerosols can enhance cloud formation at the hurricane periphery via enhancing the convection
66 over there, suppress the convection over the eyewall and therefore weaken the hurricane intensity.
67 Another recent observational analysis also corroborated that anthropogenic aerosols enlarge the
68 rainfall area of TCs over the northwestern Pacific (Zhao et al., 2018). However, the aerosol
69 microphysical effects are not represented in most operational forecast, such as the Hurricane -
70 Weather Research and Forecasting (HWRF), models, since the number concentrations of
71 CCN/cloud droplets are prescribed in the microphysics schemes in simulating cloud formation and
72 development in TCs (Zhang et al., 2018). Additionally, the pristine maritime level of the
73 CCN/cloud droplets prescribed in those models (Zhang et al., 2018) greatly underrepresented the
74 aerosol condition over land (Zhang et al., 2015). In addition to being a major metropolitan area for
75 New Orleans, the coastal areas along the Gulf of Mexico host many industrial facilities, i.e., power
76 plants, chemical manufactories, and petroleum refineries with large industrial emissions of
77 anthropogenic aerosols (Fan et al., 2005; Fan et al., 2006; Levy et al., 2013), which have been
78 shown to considerably influence convection, lightning, and precipitation (Orville et al., 2001; Fan
79 et al., 2007a, b; Li et al., 2009).

80 Air-sea interaction represents another crucial determinant factor of TC storm intensity and
81 structure (Black et al., 2007; Emanuel, 1986; Green and Zhang, 2014; Liu et al., 1979). One such
82 typical air-sea interaction is the Ekman upwelling cooling as TCs pass by the ocean, which can
83 lead to negative feedback to storm intensity because the cooler deep ocean temperature underneath
84 the TC storm suppresses heat and moisture transfer from the ocean surface to the storm circulation
85 and eventually weakens storm (Bender et al., 1993; Khain and Ginis, 1991; Ma et al., 2013; Schade
86 & Emanuel, 1999). The weakening effect due to upwelling cooling is particularly significant for



87 slowly-moving storms. In addition to modulating storm intensity, the change of SST can also alter
88 storm size and precipitation features (Chavas et al., 2016; Lin et al., 2015). As such, an inclusion
89 of air-sea interaction into models could have profound impacts on TC simulations (Bender and
90 Ginis, 2000).

91 Most of previous modeling studies adopted either fixed or prescribed SST from reanalysis
92 data to drive TC simulations (e.g., Zhang et al., 2009; Rosenfeld et al., 2011; Wang et al., 2014),
93 likely leading to significant biases in evaluating aerosol effects on TC storms due to the absence
94 of ocean feedbacks. Recently, Lynn et al. (2016) and Khain et al. (2016) found that both aerosols
95 and ocean coupling show significant effects on Hurricane Irene development, particularly on the
96 timing of hurricane's intensity evolution; but their use of 1-D ocean model coupled with WRF
97 appears underestimates the SST cooling produced by the hurricane by about 1°C relative to
98 observation. One plausible reason is that the 1-D ocean model may be unable to accurately
99 represent three-dimension physical processes in the ocean mixing layer, such as convergence and
100 its associated upwelling as TC passes (Yablonsky and Ginis, 2009). Therefore, a 3-D ocean model
101 coupled with the atmosphere model is a more advanced tool to obtain more accurate upwelling
102 cooling and thereby more accurate aerosol effect on TC power.

103 Missing of air-sea interaction introduces biases into TC simulations, and there is still lack
104 of studies on the aerosol effect on TC with ocean coupling. Therefore, it is necessary to improve
105 the understanding of how ocean coupling interacts with TC evolutions under external forcing, and
106 if the ocean coupling plays a role, to what extent it can modify the aerosol effect on TC
107 development. Therefore, the primary purpose of this study is to evaluate the ocean feedbacks
108 following aerosol microphysical effects, particularly from storm's damage perspective, including
109 precipitation and storm surge. To address these questions, we need an advanced modeling tool to



110 accurately capture air-sea interactions, particularly the SST response in simulations. In this regard,
111 we employ a 3-D atmosphere-ocean coupled cloud-resolving model, i.e., the advanced WRF
112 version 3.6 (Skamarock and Klemp, 2008) coupled with the Regional Ocean Modeling System
113 (Patricola et al., 2012) to simulate the evolution of Hurricane Katrina (2005) with a full
114 consideration of air-sea interactions. The aerosol microphysical effect on the TC destructiveness
115 is explicitly evaluated using an aerosol-aware two-moment bulk microphysical scheme (Li et al.,
116 2008). Moreover, we evaluate the role of ocean coupling in the aerosol-hurricane system and the
117 aerosol-induced ocean feedback by comparing coupled simulations with delicately designed
118 uncoupled simulations.

119 **2. Model and Experiments**

120 The aerosol-aware two-moment bulk microphysical scheme, developed at Texas A&M
121 University (hereafter referred to as the TAMU scheme), is implemented into WRF to represent
122 thirty-two microphysical processes and aerosol-cloud interactions (Li et al., 2008). The TAMU
123 scheme has been employed to evaluate the aerosol microphysical effect on various systems,
124 including mesoscale convective system (Wang et al., 2011), squall line (Li et al., 2009), TC (Wang
125 et al., 2014), and continental cloud complex (Lin et al., 2016; Wang et al., 2018). The scheme
126 contains five hydrometeor categories, i.e., cloud droplet, rain drop, ice crystal, snow, and graupel.
127 The cloud droplet number concentration is prognostically predicted through the formation from
128 the aerosol activation based on the Köhler theory and the water vapor supersaturation computed
129 by WRF. More detailed descriptions of TAMU scheme can be found in Li et al. (2008). The effect
130 of ice nuclei particles is not considered in the microphysical scheme used in our model.

131 Both WRF and ROMS are configured on the same Arakawa C grid at 3-km resolution yet
132 with 50 and 35 vertical levels, respectively. The horizontal grid spacing of 3 km fulfills the



133 minimum requirement to represent the dynamical and microphysical responses of hurricanes to
134 aerosols (Rosenfeld et al., 2012). The WRF simulation domain covers the entire Mexico Gulf and
135 the southern portion of the United States (75° W – 100° W; 17° N – 38° N) and a slightly smaller
136 domain is configured for ROMS (Fig. 1a). The atmospheric initial and boundary conditions for
137 WRF are set up by interpolating the data of the 6-hourly NCEP Climate Forecast System
138 Reanalysis (CFSR, Saha et al., 2010) to the 3-km WRF grid for the simulation period from August
139 27 to August 31 2005. The initial and boundary conditions for ROMS simulations of the same
140 period of time are specified using the Hybrid Coordinate Ocean Model (HYCOM,
141 <https://hycom.org/>) Gulf of Mexico Reanalysis dataset with a horizontal resolution of $1/25^{\circ}$. The
142 same dataset is used to provide the SST over the oceanic regions outside of the ROMS domain.

143 We carry out three primary experiments to examine the combined effects of aerosols and
144 air-sea coupling and to compare their relative importance in an aerosol-hurricane-ocean coupled
145 system. Based on the Moderate Resolution Imaging Spectroradiometer (MODIS) aerosol optical
146 depth (AOD) measurements, averaged over the periods prior to and during Hurricane Katrina
147 passage in 2005 over the Gulf of Mexico (Aug. 24 – Aug. 31), it was found that there is a clear
148 land-ocean contrast in aerosol spatial distribution (Fig. 1a), i.e., the concentration over land is two
149 folds of that over ocean for all the simulations. As such, the horizontal distribution of the initial
150 aerosol number concentration in simulations mimics the land-ocean contrast as observed in AOD
151 distribution. Over land and ocean, the aerosol concentration was uniformly distributed. The initial
152 and boundary aerosol concentration setups for both clean and polluted conditions are following
153 Wang et al. (2014). The three experiments in this study are listed in Table 1: (1) the coupled
154 experiment with the initial and boundary aerosol concentration of 200 cm^{-3} (100 cm^{-3}) over land
155 (ocean) at the surface level, representing typical clean maritime environment (hereafter C_C case);



156 (2) the coupled experiment with the aerosol's initial and boundary concentrations of 1000 cm^{-3}
157 (500 cm^{-3}) over land (ocean) (hereafter P_C case), as shown in Fig. 1b; and (3) the uncoupled
158 experiment with prescribed SST obtained from the C_C case and aerosol settings the same as the
159 P_C case (hereafter P_UC case), which is together with P_C case to isolate the aerosol-induced
160 ocean feedbacks on TC development. As such, the initial aerosol concentrations in all polluted
161 simulations are five times higher than that in all clean cases. With similar model configuration,
162 Wang et al. (2014) reported that the five times of aerosol concentration contrast between clean and
163 polluted conditions show clear aerosol effect signature in tropical cyclone development. In order
164 to evaluate the impacts of ocean coupling itself on TC responses to aerosol loadings, we perform
165 an additional pair of non-coupling simulations, namely C_UC_HYCOM and P_UC_HYCOM, in
166 which the SST is fixed and constrained by the HYCOM dataset and with the exactly same aerosol
167 settings as the pair of coupled simulations, i.e., C_C and P_C (Table 1). To mimic the emissions
168 from the continent, aerosols can be continuously advected from the lateral boundaries (Khain et
169 al., 2010). An exponential decreasing profile is assumed for the initial aerosol vertical distribution,
170 following Wang et al. (2014) and similar as Khain et al. (2016).

171 Ammonium sulphate ($(\text{NH}_4)_2\text{SO}_4$) is assumed as the chemical component of polluted continental
172 aerosols. In addition, given that sea salt is an important source of giant CCN in the central zone of
173 the storm (Rosenfeld et al., 2012), in this study we parameterize the emissions of sea salt (NaCl)
174 as a function of surface wind speed, following Binkowski and Roselle (2003) and Zhang (2005).
175 The initial concentration of sea salt is set equal to 100 cm^{-3} for all simulations, consistent with
176 Khain et al. (2016) and Lynn et al. (2016). As the hurricane develops, more sea salt particles are
177 generated by surface wind turbulence at the vicinity of the storm eyewall than the outside regions,
178 since the strengthening wind near the hurricane eyewall leads to more sea salt spray. Recent studies



179 suggest that sea salt particles may play appreciable role in altering tropical cyclones (Shpund et
180 al., 2019; Shi et al., 2021). For instance, Shpund et al. (2019) reveals that these sea salt particles
181 can give rise of additional droplets in the eyewall and may lead to a positive feedback in which
182 TC intensifies with the increase in the maximum wind. However, this effect is not taken into
183 account in this study yet as our focus is on the effect of polluted continental aerosols. The simulated
184 AOD in polluted case is about 0.55 at the domain boundaries and about 0.20 averaged over the
185 inner domain, comparable to the MODIS measurements in the Gulf of Mexico and the nearby
186 coastal regions. Also, the observed aerosol mass concentration over the Gulf of Mexico region is
187 reported about 7 g m^{-3} from the field measurements (Bate et al., 2008; Levy et al., 2013), consistent
188 with the polluted cases in this study. In addition, during hurricane development, e.g., at around
189 18:00 UTC, 27 August 2005 when MODIS measurements are available (not shown), it is found
190 that the simulation and the MODIS retrieval show similarity in spatial and clear aerosol bands
191 from the continent intruding into the storm system over the ocean.

192 To properly isolate each individual effect of aerosols and ocean feedback from their
193 combined effect, we examine the aerosol effect on TCs with and without proper ocean feedback
194 by comparing the coupled simulations (C_C and P_C cases) with an uncoupled one prescribed
195 with the SST obtained from our coupled C_C case. The combined effects of aerosol and ocean
196 coupling can be manifested by the differences between P_C and C_C. The independent effect of
197 the aerosol can be estimated by contrasting P_UC and C_C given that the SST is identical in these
198 two cases. The aerosol-modified ocean feedback, i.e., the modified ocean response to TCs when
199 the aerosol effect is present, can be assessed by the differences between the results of the P_C and
200 P_UC cases. Besides the aerosol-induced ocean responses, we are also interested in how and to
201 what extent the ocean coupling can modify the aerosol effect on TC storm. In this regard, we



202 perform comparison of the differences between the changes of the non-coupling simulations (i.e.,
203 P_UC_HYCOM - C_UC_HYCOM) and the changes of the coupled simulations (i.e.,
204 P_UC_HYCOM - C_UC_HYCOM).

205 **3. Results**

206 **3.1 Upwelling cooling and storm intensity**

207 The WRF-ROMS model used in this study in general performs well in modeling Hurricane
208 Katrina when comparing against observations. For example, the simulated storm track of the
209 hurricane shows a good agreement with the best track from NHC, particularly on 28-29 August,
210 2005 (Fig. S1a). The radius of maximum wind (RMW) of the polluted storms on 29 August, 2005
211 falls in the observed range between 45-55 km (Fig. S1b; NHC, 2023). The simulations generally
212 reproduce the typical features of Katrina evolution in terms of minimal sea-level pressure (SLP)
213 and maximum surface wind speed (Figs. 2a and b), but the peak time is somehow delayed in both
214 coupled or uncoupled polluted cases.

215 The model also well captures the spatial shape of the cold band observed after Katrina
216 passed the Gulf of Mexico, as evident in the good match of the simulated SST cooling with the
217 remote sensing observations (Fig. S2). Also, it shows better performance than the reanalysis data
218 of HYCOM (Figs. S2e and h). Since the hurricane track of the polluted coupled case (P_C)
219 generally follows that of the clean coupled case (C_C), the aerosol-modified ocean feedback in
220 upwelling cooling can be approximately estimated by subtracting the simulated SST of the C_C
221 case from that of the P_C case. Fig. S2k displays the overall SST cooling difference between the
222 P_C case and the C_C case just before Katrina's landfall in New Orleans. The spatial pattern of
223 the SST difference following the passages of the two simulated hurricanes demonstrates a slightly
224 lagged ocean response, which shows that aerosols cause the changes in hurricane that further



225 induce less upwelling cooling (positive SST difference) near the storm inner core but more cooling
226 away from the storm center. The upwelling coolings become discernible after 10 hours of the
227 WRF-ROMS coupled simulations in both experiments with different aerosol concentrations (Figs.
228 3a and b). During the period of 10-30 hour, the azimuthally mean SST difference between the P_C
229 case and the C_C case shows weak positive and negative patches changing irregularly with time
230 (Fig. 3c). Such an irregular pattern of the SST difference mainly results from the slightly southward
231 shift (about 20-30 km) of a more wobbling hurricane track in the P_C case compared to the C_C
232 case (Fig. S1a). In addition, the negative SST anomalies between 10–30 hour are likely due to the
233 track shift (blue and red solid curves in Fig. S2k) and the different storm translation speeds between
234 the two cases (blue and red solid lines in Fig. 3c). The storm translation affects SST since the
235 upwelling of cold deep ocean water would take a longer time when the storm moves more slowly.
236 As the storm moves forward, the SST responses induced by aerosols become more significant
237 during 30-55 hour, with notable less cooling over the region close to the storm inner core (< 50
238 km from the storm center) while more cooling over the region where the storm periphery locates
239 (100 km away from the storm center).

240 As for the storm intensity, the uncoupled clean case with prescribed HYCOM SST (i.e.,
241 C_UC_HYCOM) simulates the strongest storm, and then the storm intensity is greatly reduced
242 under polluted condition even without ocean coupling (i.e., P_UC_HYCOM), which is associated
243 with the aerosol weakening effect similar as proposed previously (Khain et al. 2008; Khain et al.
244 2010; Rosenfeld et al., 2012; Wang et al., 2014). The advanced atmosphere-ocean coupled
245 modeling framework enable us to assess the ocean coupling effect and its feedback caused by the
246 aerosol effect on TC. Figs. 3a and b show that the simulated storm intensity can be further
247 significantly reduced by the ocean coupling effect under both clean and polluted conditions. To



248 quantify the ocean coupling impact on the aerosol weakening effect, we derive the differences in
249 minimal SLP and maximal surface wind speed between the clean and polluted simulations for the
250 both uncoupled and coupled simulations pairs (Figs. 3c and d). It is found that the differences in
251 minimal SLP and maximal surface wind speed for the coupled and uncoupled simulation pairs are
252 similar before about 50 hours, indicating that the ocean coupling effect does not exert marked
253 impacts on the storm intensity change caused by the aerosol effect at the storm developing and
254 mature stages. As the storm starts to dissipate after 48 hours, the difference in minimal SLP
255 (maximal surface wind speed) for the coupled simulation pair is larger (more negative) than the
256 uncoupled simulation pair. In other words, the ocean coupling effect at the storm dissipating stage
257 can sustain a longer and more significant aerosol weakening effect than the case without ocean
258 coupling. In fact, the aerosol effect for the uncoupled simulations diminishes quickly as TC
259 dissipates as the difference caused by the aerosol effect decreases to zero with a relatively large
260 rate (Fig. 3c).

261 The differences between the two polluted cases with and without ocean coupling (P_C and
262 P_UC) denote the ocean coupling feedbacks following aerosol microphysical effects since both
263 cases contain the aerosol weakening effect associated with the similar loading of aerosol pollution.
264 Before the storm reaches its peak the minimal SLP and maximal surface wind speed of P_UC is
265 slightly larger than P_C and this trend is reversed during the short period just after the storm peak.
266 However, the relatively small differences in minimal SLP and maximal surface wind speed
267 between P_UC and P_C indicate that the aerosol-modified ocean coupling feedbacks does not play
268 a major role in modulating TC's peak intensity/strength.



269 3.2 Precipitation

270 The simulated TC exhibits distinct structures in terms of rainbands under the three aerosol
271 and ocean coupling scenarios (Fig. 4). The TC simulated in the two polluted cases (i.e., P_UC and
272 P_C) exhibits invigorated rainbands at the developing state (24 h), and these effects become more
273 evident when the TC approaches toward the land under higher aerosol concentrations as shown in
274 Fig. 4 at 46 h and 52 h. The invigorated rainbands in the two polluted cases are associated with a
275 weakened storm intensity and delayed storm intensification, as shown in the lower (higher) peak
276 (nadir) maximum surface wind speed (minimum sea level pressure), and the slower increase
277 (decrease) in maximum surface wind speed (minimum sea level pressure) in Figs. 3a and b. The
278 intensification of the rainbands under the polluted condition also accelerates the formation of the
279 double-eyewall structure, which is about 6 h earlier (at around 46 h) than in the C_C case (at 52 h,
280 Fig. 5a). The inner eyewall in the two polluted cases eventually dissipates at the landfall (60 h)
281 since most of the moisture and angular momentum are used to sustain the outer eyewall, resulting
282 in a singular larger eye. Overall, the two polluted cases exhibit noticeably enlarged storm size and
283 enhanced precipitation rate near the eyewall when approaches the land, consistent with previous
284 studies (e.g., Khain et al. 2010, Rosenfeld et al. 2012, Wang et al. 2014, etc.).

285 Although the aerosol-modified ocean coupling feedbacks is minor factor affecting TC's
286 peak intensity/strength, it significantly changes the precipitation distribution, leading to a more
287 contracted rainband and further enhanced precipitation rate near the eyewall, e.g., an annulus
288 heavy rain belt locates at around 60-80 km away from the TC center at the landfall (60 h) under
289 P_C case (Fig. 4c).

290 The TC storm with possible enhanced storm surge and precipitation rate near the TC
291 landfall can both significantly increase the disastrous threat of coastal flooding, which is the most



292 damaging aspect of TC impacts in coastal regions (Woodruff et al., 2013). A further examination
293 of the temporal and spatial evolution of the precipitation rate reveals that the aerosol-modified
294 ocean coupling effect can significantly change precipitation distribution and enhance precipitation
295 rate within 100 km of the TC center when TC approaches toward the land (45-60 h, Figs. 5a and
296 c). Both two polluted cases exhibit increased azimuthally-averaged profiles precipitation rate
297 primarily at 60-100 km away from the TC center, especially under the P_C case (Fig. 5d). Flooding
298 is largely determined by accumulated precipitation within certain areas and time. To assess the
299 flooding severity, we calculate the total accumulated precipitation within 100 km of the TC center,
300 particularly during the period of the TC approaching toward the land. As shown in Fig. 5e, the
301 total precipitation during the mature stage of TC on average increases by 22% in P_C case and
302 11% in P_UC relative to C_C, indicating a higher flooding potential under elevated aerosol
303 conditions, especially with the consideration of ocean coupling.

304 **3.3 Storm surge**

305 To further assess the aerosol impact on storm surge and strong wind damage, the storm
306 destructiveness potential is calculated by taking both TC intensity and TC influenced marine wind
307 fields into account. The integrated kinetic energy (IKE_{TS}) index is used here as a proxy for the
308 hurricane destructive potential (Emanuel, 2005). It is the summation of the squares of all grid cell
309 with marine winds greater than the tropical storm force wind (i.e., 18 m s^{-1}) multiplying the volume
310 with a vertical depth of 1 m centered at the 10 m-level layer. While high aerosol concentrations
311 weaken the intensity of the storm (assessed by point values like max wind or min SLP), our
312 simulations reveal an enhanced destructive power of the storm together with an increased storm
313 surge under elevated aerosol conditions (Figs. 6 and 7). As shown in Fig. 6a, the polluted cases
314 release more destructive energy than the clean one, particularly at the Katrina's landfall (at 60 h).



315 For example, the P_C case releases 11 TJ more kinetic energy than the C_C case. On average, the
316 IKE_{TS} for P_C is 18% higher than C_C over the entire hurricane lifecycle. The enhanced storm
317 destructiveness is attributed to the expansion of the storm circulation (Figs. 6b) to produce higher
318 surface winds beyond the eyewall region and a larger area of tropical storm force (Fig. 8a). With
319 the ocean coupling, the IKE_{TS} for P_C slightly decreases by less than 5% relative to P_UC as the
320 storm approaches to land. From Fig. 8b it is also found that the wind outside of the eyewall is
321 stronger in P_UC than P_C from hour 50 to 60, which is responsible for the higher destructiveness
322 in P_UC at this time period. This also suggests that ocean coupling plays a minor role in
323 modulating the damages corresponding to strong wind and storm surge.

324 As a direct indicator of storm surge, the sea level height is simulated with the integration
325 of the 3-D ocean model ROMS (Fig. 7). Our simulation generally captures the peak timing and
326 magnitude of observed sea level height at Dauphin Island, AL (Fig. 7a). Albeit the insufficient
327 gauge measurement at other stations, the simulated peak sea level heights are comparable to the
328 recorded values at New Canal and Shell Beach stations (Fritz et al., 2008). The polluted TC can
329 produce a more than 50 cm higher storm surge than the clean one (Figs. 7 and 9a), suggesting that
330 the TC likely causes more severe damage by storm surge along the coastal area under polluted
331 condition than clean condition. Since storm surge is caused primarily by the strong winds in
332 tropical storm, we derive three snapshots of the wind speed difference between the coupled
333 polluted and clean simulations over New Orleans coastal area when Katrina passed over (Fig. 9b).
334 The stronger surface wind (i.e., positive difference in wind speed) cyclonically around the storm
335 are found at certain shore region, e.g., near Shell Beach and Dauphin Island. The enhanced wind
336 can push more water toward the shore, and more water can pile up over the shore, eventually
337 leading to more severe storm surge under the polluted condition.



338 **3.4 Storm structure redistribution**

339 The modifications on precipitation characteristics and storm destructiveness by aerosols
340 are mainly due to storm intensity changes and structural redistribution under the high aerosol
341 scenarios. The underlying physical mechanism can be further revealed by examining the vertical-
342 radial cross-sections of the dynamic and thermodynamic of the storm (Fig. 10). By serving as
343 CCNs, the elevated aerosols tend to suppress warm rain process and invigorate mixed- and ice-
344 phase clouds in outer rainbands and significantly change latent heat distribution. As shown in Fig.
345 10a, P_C case exhibits higher ice water content (IWC) in outer rainbands and a more divergent
346 latent heating distribution with reduced latent heating near the eyewall and enhanced latent heating
347 over the area 40-100 km away from the storm center.

348 The enhanced heat flux outward the eyewall is associated with the enhanced propagation
349 of vortex Rossby waves (VRWs) which accelerate the tangential winds near the RMW of the
350 polluted storm (Figs. S3 and 4). The VRWs theories have been widely used to explain the storm
351 intensity and structural changes, as well as the formation of spiral rainband in TC (Houze et al.,
352 2007; Montgomery and Kallenbach, 1997; Wang, 2002). The enhanced outward propagation of
353 VRWs under polluted cases transport more angular momentum from the eyewall to the outer
354 rainbands, accelerating tangential wind in the rainbands at the cost of decelerating the tangential
355 wind in the eyewall (Figs. S3 and 4). A further examination of the corresponding potential vorticity
356 (PV) field shows that aerosol can significantly change the vortex structure by weakening its overall
357 vorticity (Fig. 10b) and subsequently reduce the β drift of the hurricane. To conserve angular
358 momentum during the vorticity rearrangement, some of the high eyewall vorticity is also fluxed
359 outward, taking on the form of outward-propagating VRWs. These waves rotate cyclonically with
360 the high PV core and propagate radially outward and stagnate at radii of 70–90 km, where the



361 radial potential vorticity gradient disappears or reverses its sign. In the polluted case, the large
362 gradient of equivalent potential temperature (θ_e) between 6-9 km suggests a more stable condition,
363 which favors the VRWs propagation outward along radial direction (Fig. 10c). Moreover, the
364 evaporative cooling of rainbands can result in significant downdrafts, which often bring cool and
365 dry air (i.e., smaller moist static energy supply) into the inflow boundary layer. For example, the
366 relative lower θ_e is observed at outer rainbands (>45 km) at 0-3 km high of the atmosphere under
367 the polluted case than the clean case by up to 3 K. The air flow with this lower moist static energy
368 might be transported and mixed into the eyewall, further contributing the weakening of the eyewall
369 convection and thus the reduction of the storm intensity.

370 Since the storm development is highly influenced by the energy gained from ocean water,
371 it is necessary to examine the dynamic and thermodynamic processes occurring at the air-sea
372 interface to further elucidate the mechanisms leading to the storm structural modifications by the
373 aerosol and ocean coupling effects. To first examine the aerosol effect on the TC evolution without
374 ocean feedback, we compare the pollutant uncoupled case (P_UC) with those of the clean coupled
375 case (C_C), both of which are forced with the same SST distribution in the model. Fig. 11a shows
376 the differences of the total surface heat flux and wind stress magnitudes between P_UC and C_C.
377 Of the most prominent feature is the significant surface heat flux deficiency (surplus) well
378 correlated with negative (positive) wind stress difference within about 25-50 km distance from the
379 storm center throughout most periods of the whole simulation, except some very brief periods of
380 time. This suggests that surface heat flux near the core region (approximately within RMS) is
381 mainly driven by the magnitude of surface wind stress rather than moisture flux difference. On the
382 other hand, over 50 km away from the center, the surface heat flux and wind stress differences in
383 the pollutant uncoupled case are all generally larger than those of the clean coupled case. The



384 significant negative surface heat flux difference around 50 to 100 km distance from the center is
385 associated with the higher surface heat flux in the clean coupled case, which arises due to the drier
386 descending air in the moat area of the double eyewall forming between hours 57 and 60.

387 Here we evaluate the impact of SST difference induced by the aerosol-contaminated TC
388 on the surface heat flux and wind stress distributions, which manifests the contributions of ocean
389 feedback to the pollutant TC aloft. Fig. 11b displays the surface heat flux and wind stress
390 differences between the pollutant coupled (P_C) and uncoupled (P_UC) cases. In general, we
391 expect to see a relatively higher SST in the wake of the TC in the pollutant cases than that in the
392 clean case due to a weaker Ekman upwelling response to a pollutant TC. However, due to the
393 discrepancy of some slight track deviation between the pollutant case and the clean coupled case,
394 some relatively lower near-center SST can also be experienced by the pollutant TC core compared
395 to the clean TC core, which thus contribute to the formation of negative surface heat flux and wind
396 stress differences, as displayed in the Hovemuller diagram. This is the case for the significant
397 surface heat flux deficit overlapping with surface wind stress deficit between hour 12 and 42,
398 which is associated with a slightly leftward deviation of the TC track in P_UC as compared with
399 that of P_C (see Fig. S1a), leading to the pollutant TC of the uncoupled case surrounded by
400 relatively cooler SST. After the TCs turn more northwards approaching the warm Loop Current
401 Eddy around 90.5 W and 27 N, the tracks of both TCs nearly always overlap with each other until
402 landfall, where more symmetrically positive (negative) SST difference near (off) the TC cores can
403 be observed (see Fig. S2 and Fig. 11b). The colocations of both the positive and negative surface
404 heat flux and wind stress differences after hour 42 well manifest a clear air-sea coupling signal:
405 the warmer (cooler) SST not only causes more (less) surface heat flux but also increase (decrease)
406 the magnitude of surface wind stress by enhancing (reducing) the turbulent momentum mixing



407 downwards from the free atmosphere to ocean surface. This further indicates that a strong Ekman
408 upwelling tends to decouple the near-surface surface flow from the flow on the top of boundary
409 layer, reducing the dynamic and thermodynamic forcing of the TC to the ocean beneath.

410 Fig. 11c shows the combined effect of aerosols and air-sea interaction on the surface heat
411 flux and wind stress distributions of the TC. The surface heat flux and wind stress differences show
412 some characteristics similar to those in Fig. 11a yet they demonstrate a better correlation with each
413 other than the pollutant case without proper ocean feedback, especially during the time from hour
414 42 to 60 before landfall. Note that the evident surface heat flux deficit before hour 60 is well
415 correlated with the wind stress deficit under the combined effect of aerosols and air-sea coupling,
416 in contrast to the result shown in Fig. 11a, in which negative surface heat flux difference is
417 collocated with positive surface wind stress difference. Of particular interest is that the seemingly
418 quasi-periodic burstings of high surface heat flux difference due to the aerosol effect (Fig. 11a)
419 turn into sporadic bursts of heat flux and wind stress anomalies in Fig. 11c, suggesting that a proper
420 air-sea coupling, as reflected by the strength of ocean feedback modulated by an aerosol-
421 contaminated TC, still plays a role in affecting the magnitudes of surface heat flux and wind stress
422 of a pollutant TC and thus its precipitation distribution moving with the TC.

423 To be more clearly quantitatively view the dynamic and thermodynamic processes
424 occurring at the air-sea interface response to aerosol and ocean coupling, we derive azimuthally-
425 averaged radial profiles at the ocean surface for the three aerosol and ocean coupling scenarios
426 averaged over two periods, i.e., the typical period of storm developing stage (15-28 hours) and the
427 typical period of storm mature stage (42-55 hours, Fig. 12). On average the lower surface heat flux
428 in P_C than P_UC at the developing stage (left column in Figs. 12a and b) is due to the relatively
429 cooler near-center SST, which is caused slight deviation of the TC track in the two polluted cases



430 in comparison with the clean case (Fig. S1). Without consideration of the track shift in P_C relative
431 to C_C case, the upwelling cooling strength in C_C case is actually very close to P_C at this stage
432 (Fig. 12b), suggesting that the change of ocean feedback strength due to the aerosol effect on the
433 TC is still not strong enough at the beginning stage to significantly impact the TC aloft. This can
434 be evidence in by the relatively small differences in surface wind stress and total water path formed
435 in the storm among the three cases (Figs. 12c and d). This is further confirmed by little changes in
436 precipitation (Fig. 5) or storm destructiveness (Fig. 6) of P_C from P_UC cases at the developing
437 stage. However, as the TC approaches toward the land with higher aerosols concentrations, the
438 ocean feedback starts to affect the evolution of the TC. At the mature stage (42-55 hr), the SST
439 feedback shows a warm core with a time average of azimuthally mean SST up to 0.5°C warmer in
440 P_C than that in C_C and a slightly colder periphery. The SST warming (cooling) near the inner
441 core (the periphery) increases (reduces) the thermal energy transfer to the storm eyewall (outer
442 rainbands). Thus, a weaker Ekman upwelling cooling near the center of the polluted TC
443 reciprocally increases the coupling between the near-surface flow and the aloft free atmosphere
444 flow, providing relatively more surface heat flux near the eyewall of the polluted TC, as positive
445 feedback to sustain the strength of the TC aloft. Consequently, the aerosol-modified ocean
446 feedback significantly enhances the cloud formation and precipitation rate near the eyewall (Figs.
447 12d and 5d). The enhanced cloud formation in turn results in larger latent heat release aloft over
448 the region just outside of 50 km away from the storm center (Fig. S5), which further strengthens
449 the cloud convection and may also contribute to the enhancement of cloud formation in the storm.

450 **4. Summary and conclusions**

451 In this study, we quantitatively assess the aerosol microphysical effect and aerosol-induced
452 ocean feedback on the development and destructiveness of a tropical cyclone (TC). For the first



453 time, a three-dimension atmosphere-ocean fully coupled regional model (WRF-ROMS) at the
454 cloud-resolving scale was used to simulate Hurricane Katrina to investigate the aerosol-TC system
455 with inclusion of air-sea interaction.

456 Our atmosphere-ocean coupled modeling framework clearly detects significant ocean
457 response in SST induced by the aerosol effect as the storm approaches to its mature stage (e.g.,
458 after 30 hours of the WRF-ROMS simulation). Moreover, our study reveals that anthropogenic
459 aerosols enlarge the air circulation of the storm as well as the rainbands with weakened storm
460 intensity and delayed storm intensification. The comparison of the aerosol weakening effect
461 between the simulations with and without ocean coupling suggests that ocean coupling can sustain
462 more significant aerosol effect at the storm dissipating stage. With an increase in aerosol
463 concentration by five times, the total precipitation within 100 km of the TC center during the
464 mature stage increases by 22% and 11% with and without ocean coupling, respectively, suggesting
465 a high flooding-potential under elevated aerosol conditions, especially with the consideration of
466 air-sea interaction. The integrated kinetic energy, which is an indicator of storm surge and strong
467 wind damage, increases by 18% from the clean to polluted aerosol conditions over the entire
468 hurricane lifecycle. The ocean feedback due to the aerosol effect (i.e., aerosol-modified ocean
469 coupling effect) on the TC intensity is minimal at the beginning stage but plays a significant role
470 in precipitation distribution, especially as the TC approaches landfall with higher aerosols
471 concentrations.

472 Our work elucidates the underlying mechanisms through which aerosols and ocean
473 coupling affect the storm structure and intensity as well as the destructive power, as depicted in
474 Fig. 13. When approaching landfall aerosols can invigorate the mixed- and ice-phase clouds in TC
475 periphery by serving as CCN with additional latent heat release aloft at the rainbands, enhancing



476 outward propagation of vortex Rossby waves from the eyewall regions. The aerosol effect also
477 induces a lower equivalent potential temperature in the inflow within the boundary layer because
478 of evaporative cooling of rainbands, leading to reduced moist static energy transited to the storm
479 center. More significant outward propagation of VRWs and less moist static energy supply leads
480 to weakening of the storm eyewall but enlarged storm circulation. With inclusion of the ocean
481 coupling effect, the Ekman upwelling cooling near the eyewall reciprocally increases the
482 interaction between the near-surface flow and the aloft free atmosphere flow, thus providing larger
483 surface heat flux near the eyewall to sustain the strength of the TC aloft. Overall, the combined
484 aerosol effects result in a noticeably enhanced precipitation rate and strengthened storm
485 destructiveness with enhanced storm surge and enlarged circulation, both significantly
486 contributing to coastal flooding.

487 Our study demonstrates that accurate prediction of TC development and destructiveness
488 requires the representation of atmosphere-ocean coupling in hurricane forecast models, because of
489 the significant Ekman upwelling cooling and its considerable feedbacks to the storm. Our results
490 show that aerosols play a prominent role in modulating the TC storm intensity and structure with
491 the inclusion of ocean coupling effect, corroborating the notion that the aerosol effects cannot be
492 neglected in the TC forecast models. Note that our modeling study assumes no time-varying
493 sources of aerosols during the model integration, which may introduce uncertainty to the simulated
494 aerosol budget. In addition, the microphysical scheme used in our model does not link ice
495 heterogeneous nucleation with the prognostic aerosols as ice-nucleating particles, and ice
496 nucleating particles have been shown to be crucial for ice phase cloud simulations in the convective
497 storms (Jin et al., 2014; Zhao et al., 2019). Future improvements in the representations of the
498 anthropogenic aerosols and their interactions with clouds in cloud-resolving models are necessary



499 to advance the understanding of the aerosol-TC system with explicit representation of the air-sea
500 interaction.

501 **Code Availability**

502 The code of WRF model used in this study is available at
503 <https://www2.mmm.ucar.edu/wrf/users/downloads.html>. For the code of ROMS, please contact
504 the corresponding authors of the paper.

505 **Data Availability**

506 The hurricane Best Track Data is from national hurricane center (NHC,
507 <https://www.nhc.noaa.gov/>). The observed sea level height data at tide stations is available at
508 <https://tidesandcurrents.noaa.gov/stations.html?type=Water+Levels>. All the WRF model
509 simulation output used for this research can be downloaded from the website at
510 <http://web.gps.caltech.edu/~yzw/share/LinY-2023-ACP>.

511 **Author Contributions**

512 Y.W. and R.Z. conceived and designed the research. Y.L., J.H., and Y.W. designed and performed
513 the model simulation. All authors contributed to the model and observational data analyses and
514 manuscript revision. Y.L., and Y.W. wrote the manuscript.

515 **Acknowledgments**

516 Y. Wang was supported by the NSF grant (award no. AGS-2103714). Additional support was
517 provided by the Welch A. Foundation (A-1417). Y. Lin was supported by the NSF grant (award
518 no., AGS-2103820) and NASA CCST (award no., 80NSSC23K0119) grant. J.H. Jiang
519 acknowledged the support of the Jet Propulsion Laboratory, California Institute of Technology,



520 under contract with NASA. Additional support was provided by the Welch A. Foundation (A-
521 1417). We also acknowledge the computational support from Texas A&M High Performance
522 Research Computing (HPRC) facility. All requests for materials in this paper should be addressed
523 to Yuan Wang (yuanwang@purdue.edu).

524 **Competing interests**

525 Y. Wang is a member of the editorial board of Atmospheric Chemistry and Physics.



526 **References**

- 527 Bates, T. S., Quinn, P. K., Coffman, D., Schulz, K., Covert, D. S., Johnson, J. E., Williams, E. J.,
528 Lerner, B. M., Angevine, W. M., Tucker, S. C., Brewer, W. A., and Stohl, A.: Boundary layer
529 aerosol chemistry during TexAQS/GoMACCS 2006: Insights into aerosol sources and
530 transformation processes, *J. Geophys. Res.*, 113, n/a-n/a, 10.1029/2008JD010023, 2008.
- 531 Bender, M. A. and Ginis, I.: Real-case simulations of hurricane-ocean interaction using a high-
532 resolution coupled model: Effects on hurricane intensity, *Mon. Weather Rev.*, 128, 917-946, Doi
533 10.1175/1520-0493(2000)128<0917:Rcsoho>2.0.Co;2, 2000.
- 534 Bender, M. A., Ginis, I., and Kurihara, Y.: Numerical simulations of tropical cyclone-ocean
535 interaction with a high-resolution coupled model, *J. Geophys. Res.*, 98, 23245-23263,
536 10.1029/93JD02370, 1993.
- 537 Binkowski, F. S. and Roselle, S. J.: Models - 3 Community Multiscale Air Quality (CMAQ)
538 model aerosol component 1. Model description, *J. Geophys. Res.*, 108,
539 doi:10.1029/2001JD001409, 2003.
- 540 Black, P. G., D'Asaro, E. A., Sanford, T. B., Drennan, W. M., Zhang, J. A., French, J. R., Niiler,
541 P. P., Terrill, E. J., and Walsh, E. J.: Air-sea exchange in hurricanes: synthesis of observations
542 from the coupled boundary layer air-sea transfer experiment, *Bull. Am. Meteorol. Soc.*, 88, 357-
543 374, 10.1175/BAMS-88-3-357, 2007.
- 544 Chavas, D. R., Lin, N., Dong, W., and Lin, Y.: Observed tropical cyclone size revisited, *J. Clim.*,
545 29, 2923-2939, 10.1175/jcli-d-15-0731.1, 2016.
- 546 Emanuel, K.: Increasing destructiveness of tropical cyclones over the past 30 years, *Nature*, 436,
547 686-688, 10.1038/nature03906, 2005.



- 548 Emanuel, K.: Assessing the present and future probability of Hurricane Harvey's rainfall, Proc.
549 Nat. Acad. Sci. U.S.A., 114, 12681-12684, 10.1073/pnas.1716222114, 2017.
- 550 Emanuel, K. A.: An air-sea interaction theory for tropical cyclones. Part I: Steady-state
551 maintenance, J. Atmos. Sci., 43, 585-605, 10.1175/1520-0469(1986)043<0585:aasitf>2.0.co;2,
552 1986.
- 553 Fan, J., Zhang, R. Y., Li, G. H., and Tao, W. K.: Effects of aerosols and relative humidity on
554 cumulus clouds, J. Geophys. Res., 112, D14204, 10.1029/2006jd008136, 2007a.
- 555 Fan, J., Zhang, R., Li, G., Tao, W.-K., and Li, X.: Simulations of cumulus clouds using a spectral
556 microphysics cloud-resolving model, J. Geophys. Res., 112, D04201, 10.1029/2006jd007688,
557 2007b.
- 558 Fan, J., Zhang, R. Y., Li, G. H., Nielsen-Gammon, J., and Li, Z. Q.: Simulations of fine
559 particulate matter (PM_{2.5}) in Houston, Texas, J. Geophys. Res., 110, D16203,
560 10.1029/2005jd005805, 2005.
- 561 Fan, J. W., Zhang, R. Y., Collins, D., and Li, G. H.: Contribution of secondary condensable
562 organics to new particle formation: A case study in Houston, Texas, Geophys. Res. Lett., 33,
563 Artn L15802, 10.1029/2006gl026295, 2006.
- 564 Fan, J. W., Rosenfeld, D., Zhang, Y. W., Giangrande, S. E., Li, Z. Q., Machado, L. A. T.,
565 Martin, S. T., Yang, Y., Wang, J., Artaxo, P., Barbosa, H. M. J., Braga, R. C., Comstock, J. M.,
566 Feng, Z., Gao, W. H., Gomes, H. B., Mei, F., Pohlker, C., Pohlker, M. L., Poschl, U., and de
567 Souza, R. A. F.: Substantial convection and precipitation enhancements by ultrafine aerosol
568 particles, Science, 359, 411-418, 10.1126/science.aan8461, 2018.



- 569 Fritz, H. M., Blount, C., Sokoloski, R., Singleton, J., Fuggle, A., McAdoo, B. G., Moore, A.,
570 Grass, C., and Tate, B.: Hurricane Katrina storm surge distribution and field observations on the
571 Mississippi Barrier Islands, *Estuar. Coast. Shelf Sci.*, 74, 12-20, 10.1016/j.ecss.2007.03.015,
572 2007.
- 573 Fritz, H. M., Blount, C., Sokoloski, R., Singleton, J., Fuggle, A., McAdoo, B. G., Moore, A.,
574 Grass, C., and Tate, B.: Hurricane Katrina storm surge reconnaissance, *J. Geotech. Geoenviron.*,
575 134, 644-656, 10.1061/(Asce)1090-0241(2008)134:5(644), 2008.
- 576 Green, B. W. and Zhang, F.: Impacts of air–sea flux parameterizations on the intensity and
577 structure of tropical cyclones, *Mon. Weather Rev.*, 141, 2308-2324, 10.1175/MWR-D-12-
578 00274.1, 2013.
- 579 Herbener, S. R., Heever, S. C. v. d., Carrió, G. G., Saleeby, S. M., and Cotton, W. R.: Aerosol
580 indirect effects on idealized tropical cyclone dynamics, *J. Atmos. Sci.*, 71, 2040-2055,
581 10.1175/jas-d-13-0202.1, 2014.
- 582 Houze, R. A., Chen, S. S., Smull, B. F., Lee, W.-C., and Bell, M. M.: Hurricane intensity and
583 eyewall replacement, *Science*, 315, 1235-1239, 10.1126/science.1135650, 2007.
- 584 Jin, Y., Wang, S. P., Nachamkin, J., Doyle, J. D., Thompson, G., Grasso, L., Holt, T., Moskaitis,
585 J., Jin, H., Hodur, R. M., Zhao, Q. Y., Liu, M., and DeMaria, M.: The Impact of Ice Phase Cloud
586 Parameterizations on Tropical Cyclone Prediction, *Mon. Weather Rev.*, 142, 606-625,
587 10.1175/Mwr-D-13-00058.1, 2014.
- 588 Khain, A., Lynn, B., and Dudhia, J.: Aerosol effects on intensity of landfalling hurricanes as seen
589 from simulations with the WRF model with spectral bin microphysics, *J. Atmos. Sci.*, 67, 365-
590 384, doi:10.1175/2009JAS3210.1, 2010.



- 591 Khain, A., Lynn, B., and Shpund, J.: High resolution WRF simulations of Hurricane Irene:
592 Sensitivity to aerosols and choice of microphysical schemes, *Atmos. Res.*, 167, 129-145,
593 <http://dx.doi.org/10.1016/j.atmosres.2015.07.014>, 2016.
- 594 Khain, A., Cohen, N., Lynn, B., and Pokrovsky, A.: Possible aerosol effects on lightning activity
595 and structure of hurricanes, *J. Atmos. Sci.*, 65, 3652-3677, 10.1175/2008JAS2678.1, 2008.
- 596 Khain, A. P. and Ginis, I.: The mutual response of a moving tropical cyclone and the ocean,
597 *Beitr. Phys. Atmos.*, 64, 125-141, 1991.
- 598 Khain, A., Lynn, B., and Dudhia, J.: Aerosol effects on intensity of landfalling hurricanes as seen
599 from simulations with the WRF model with spectral bin microphysics, *J. Atmos. Sci.*, 67, 365-
600 384, doi:10.1175/2009JAS3210.1, 2010.
- 601 Knutson, T., Camargo, S. J., Chan, J. C. L., Emanuel, K., Ho, C. H., Kossin, J., Mohapatra, M.,
602 Satoh, M., Sugi, M., Walsh, K., and Wu, L. G.: Tropical cyclones and climate change
603 assessment: Part I: detection and attribution, *Bull. Am. Meteorol. Soc.*, 100, 1987-2007,
604 10.1175/Bams-D-18-0189.1, 2019.
- 605 Levy, M. E., Zhang, R. Y., Khalizov, A. F., Zheng, J., Collins, D. R., Glen, C. R., Wang, Y., Yu,
606 X. Y., Luke, W., Jayne, J. T., and Olaguer, E.: Measurements of submicron aerosols in Houston,
607 Texas during the 2009 SHARP field campaign, *J. Geophys. Res.*, 118, 10518-10534,
608 10.1002/Jgrd.50785, 2013.
- 609 Levy, R. C., Leptoukh, G. G., Kahn, R., Zubko, V., Gopalan, A., and Remer, L. A.: A critical
610 look at deriving monthly aerosol optical depth from satellite data, *IEEE Trans. Geosci. Remote*
611 *Sens.*, 47, 2942-2956, Doi 10.1109/Tgrs.2009.2013842, 2009.



- 612 Li, G., Wang, Y., and Zhang, R.: Implementation of a two-moment bulk microphysics scheme to
613 the WRF model to investigate aerosol-cloud interaction, *J. Geophys. Res.*, 113, D15211,
614 10.1029/2007jd009361, 2008.
- 615 Li, G., Wang, Y., Lee, K.-H., Diao, Y., and Zhang, R.: Impacts of aerosols on the development
616 and precipitation of a mesoscale squall line, *J. Geophys. Res.*, 114, D17205,
617 10.1029/2008jd011581, 2009.
- 618 Lin, Y., Zhao, M., and Zhang, M.: Tropical cyclone rainfall area controlled by relative sea
619 surface temperature, *Nature Communications*, 6, 6591, 10.1038/ncomms7591, 2015.
- 620 Lin, Y., Wang, Y., Pan, B., Hu, J., Liu, Y., and Zhang, R.: Distinct Impacts of Aerosols on an
621 Evolving Continental Cloud Complex during the RACORO Field Campaign, *J. Atmos. Sci.*, 73,
622 3681-3700, 10.1175/jas-d-15-0361.1, 2016.
- 623 Liu, W. T., Katsaros, K. B., and Businger, J. A.: Bulk parameterization of air-sea exchanges of
624 heat and water vapor including the molecular constraints at the interface, *J. Atmos. Sci.*, 36,
625 1722-1735, 10.1175/1520-0469(1979)036<1722:bpoase>2.0.co;2, 1979.
- 626 Lynn, B. H., Khain, A. P., Bao, J. W., Michelson, S. A., Yuan, T., Kelman, G., Rosenfeld, D.,
627 Shpund, J., and Benmoshe, N.: The sensitivity of hurricane Irene to aerosols and ocean coupling:
628 simulations with WRF spectral bin microphysics, *J. Atmos. Sci.*, 73, 467-486, 10.1175/jas-d-14-
629 0150.1, 2016.
- 630 Ma, Z., Fei, J., Liu, L., Huang, X., and Cheng, X.: Effects of the cold core eddy on tropical
631 cyclone intensity and structure under idealized air-sea interaction conditions, *Mon. Weather*
632 *Rev.*, 141, 1285-1303, 10.1175/mwr-d-12-00123.1, 2013.



- 633 Montgomery, M. T. and Kallenbach, R. J.: A theory for vortex Rossby-waves and its application
634 to spiral bands and intensity changes in hurricanes, Q. J. Roy. Meteorol. Soc., 123, 435-465, DOI
635 10.1002/qj.49712353810, 1997.
- 636 NWS (National Weather Service): A theory for vortex rossby-waves and its application to spiral
637 bands and intensity changes in hurricanes, <https://www.weather.gov/mob/katrina>, 2016.
- 638 Orville, R. E., Huffines, G., Nielsen-Gammon, J., Zhang, R. Y., Ely, B., Steiger, S., Phillips, S.,
639 Allen, S., and Read, W.: Enhancement of cloud-to-ground lightning over Houston, Texas,
640 Geophys. Res. Lett., 28, 2597-2600, Doi 10.1029/2001gl012990, 2001.
- 641 Pan, B., Wang, Y., Hu, J., Lin, Y., Hsieh, J.-S., Logan, T., Feng, X., Jiang, J. H., Yung, Y. L.,
642 and Zhang, R.: Impacts of Saharan dust on Atlantic regional climate and implications for tropical
643 cyclones, J. Clim., 31, 7621-7644, 10.1175/jcli-d-16-0776.1, 2018.
- 644 Pan, B. W., Wang, Y., Logan, T., Hsieh, J. S., Jiang, J. H., Li, Y. X., and Zhang, R. Y.:
645 Determinant role of aerosols from industrial sources in hurricane Harvey's catastrophe, Geophys.
646 Res. Lett., 47, ARTN e2020GL090014, 10.1029/2020GL090014, 2020.
- 647 Patricola, C. M., Chang, P., Li, M., Saravanan, R., Xu, Z., and Hsieh, J.-S.: An investigation of
648 tropical Atlantic bias in a high-resolution coupled regional climate model, Climate Dynamic,
649 10.1007/s00382-012-1320-5, 2012.
- 650 Richard, D., Rhome, R., and Brown, P.: Hurricane Katrina (PDF) (Report). Tropical Cyclone
651 Report. National Hurricane Center, https://www.nhc.noaa.gov/data/tcr/AL122005_Katrina.pdf,
652 December 20, 2005 (accessed on April 23, 2023).
- 653 Rosenfeld, D., Clavner, M., and Nirel, R.: Pollution and dust aerosols modulating tropical
654 cyclones intensities, Atmos. Res., 102, 66-76, 10.1016/j.atmosres.2011.06.006, 2011.



- 655 Rosenfeld, D., Woodley, W. L., Khain, A., Cotton, W. R., Carrió, G., Ginis, I., and Golden, J.
656 H.: Aerosol effects on microstructure and intensity of tropical cyclones, *Bull. Am. Meteorol.*
657 *Soc.*, 10.1175/BAMS-D-11-00147.1, 2012.
- 658 Saha, S., Moorthi, S., Pan, H.-L., Wu, X., Wang, J., Nadiga, S., Tripp, P., Kistler, R., Woollen,
659 J., Behringer, D., Liu, H., Stokes, D., Grumbine, R., Gayno, G., Wang, J., Hou, Y.-T., Chuang,
660 H.-y., Juang, H.-M. H., Sela, J., Iredell, M., Treadon, R., Kleist, D., Delst, P. V., Keyser, D.,
661 Derber, J., Ek, M., Meng, J., Wei, H., Yang, R., Lord, S., Dool, H. v. d., Kumar, A., Wang, W.,
662 Long, C., Chelliah, M., Xue, Y., Huang, B., Schemm, J.-K., Ebisuzaki, W., Lin, R., Xie, P.,
663 Chen, M., Zhou, S., Higgins, W., Zou, C.-Z., Liu, Q., Chen, Y., Han, Y., Cucurull, L., Reynolds,
664 R. W., Rutledge, G., and Goldberg, M.: The NCEP climate forecast system reanalysis, *Bull. Am.*
665 *Meteorol. Soc.*, 91, 1015-1058, 10.1175/2010bams3001.1, 2010.
- 666 Schade, L. R. and Emanuel, K. A.: The ocean's effect on the intensity of tropical cyclones:
667 Results from a simple coupled atmosphere–ocean model, *J. Atmos. Sci.*, 56, 642-651,
668 10.1175/1520-0469(1999)056<0642:toseot>2.0.co;2, 1999.
- 669 Shpund, J., Khain, A., and Rosenfeld, D.: Effects of Sea Spray on Microphysics and Intensity of
670 Deep Convective Clouds Under Strong Winds, *J. Geophys. Res.*, 124, 9484-9509,
671 10.1029/2018jd029893, 2019.
- 672 Shi, J. J., Braun, S. A., Tao, Z., and Matsui, T.: Influence of the Saharan Air Layer on Hurricane
673 Nadine (2012). Part I: Observations from the Hurricane and Severe Storm Sentinel (HS3)
674 Investigation and Modeling Results, *Mon. Weather Rev.*, 149, 3541-3562,
675 <https://doi.org/10.1175/MWR-D-20-0344.1>, 2021.



- 676 Skamarock, W. C. and Klemp, J. B.: A time-split nonhydrostatic atmospheric model for weather
677 research and forecasting applications, *J Comput Phys*, 227, 3465-3485,
678 <https://doi.org/10.1016/j.jcp.2007.01.037>, 2008.
- 679 Trenberth, K. E., Cheng, L. J., Jacobs, P., Zhang, Y. X., and Fasullo, J.: Hurricane Harvey links
680 to ocean heat content and climate change adaptation, *Earths Future*, 6, 730-744,
681 [10.1029/2018ef000825](https://doi.org/10.1029/2018ef000825), 2018.
- 682 van Oldenborgh, G. J., van der Wiel, K., Sebastian, A., Singh, R., Arrighi, J., Otto, F., Haustein,
683 K., Li, S. H., Vecchi, G., and Cullen, H.: Attribution of extreme rainfall from Hurricane Harvey,
684 August 2017, *Environ. Res. Lett.*, 12, ARTN 124009, [10.1088/1748-9326/aa9ef2](https://doi.org/10.1088/1748-9326/aa9ef2), 2017.
- 685 Wang, Y., Lee, K.-H., Lin, Y., Levy, M., and Zhang, R.: Distinct effects of anthropogenic
686 aerosols on tropical cyclones, *Nature Climate Change*, 4, 368-373, [10.1038/nclimate2144](https://doi.org/10.1038/nclimate2144), 2014.
- 687 Wang, Y., Wan, Q., Meng, W., Liao, F., Tan, H., and Zhang, R.: Long-term impacts of aerosols
688 on precipitation and lightning over the Pearl River Delta megacity area in China, *Atmos. Chem.*
689 *Phys.*, 11, 12421-12436, [10.5194/acp-11-12421-2011](https://doi.org/10.5194/acp-11-12421-2011), 2011.
- 690 Wang, Y., Vogel, J. M., Lin, Y., Pan, B., Hu, J., Liu, Y., Dong, X., Jiang, J. H., Yung, Y. L., and
691 Zhang, R.: Aerosol microphysical and radiative effects on continental cloud ensembles, *Adv.*
692 *Atmos. Sci.*, 35, 234-247, [10.1007/s00376-017-7091-5](https://doi.org/10.1007/s00376-017-7091-5), 2018.
- 693 Wang, Y. Q.: Vortex Rossby waves in a numerically simulated tropical cyclone. Part II: The role
694 in tropical cyclone structure and intensity changes, *J. Atmos. Sci.*, 59, 1239-1262, [10.1175/1520-0469\(2002\)059<1239:Vrwian>2.0.Co;2](https://doi.org/10.1175/1520-0469(2002)059<1239:Vrwian>2.0.Co;2), 2002.
- 696 Woodruff, J. D., Irish, J. L., and Camargo, S. J.: Coastal flooding by tropical cyclones and sea-
697 level rise, *Nature*, 504, 44-52, [10.1038/nature12855](https://doi.org/10.1038/nature12855), 2013.



698 Yablonsky, R. M. and Ginis, I.: Limitation of one-dimensional ocean models for coupled
699 hurricane–ocean model forecasts, *Mon. Weather Rev.*, 137, 4410–4419,
700 10.1175/2009mwr2863.1, 2009.

701 Zhang, H., McFarquhar, G. M., Cotton, W. R., and Deng, Y.: Direct and indirect impacts of
702 Saharan dust acting as cloud condensation nuclei on tropical cyclone eyewall development,
703 *Geophys. Res. Lett.*, 36, n/a–n/a, 10.1029/2009GL037276, 2009.

704 Zhang, K. M., Knipping, E. M., Wexler, A. S., Bhave, P. V., and Tonnesen, G. S.: Size
705 distribution of sea-salt emissions as a function of relative humidity, *Atmos. Environ.*, 39, 3373–
706 3379, <https://doi.org/10.1016/j.atmosenv.2005.02.032>, 2005.

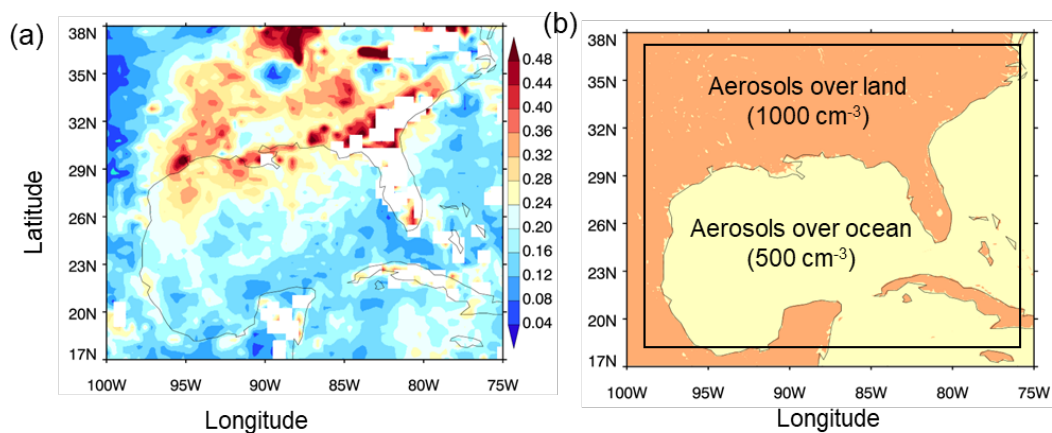
707 Zhang, R., Wang, G., Guo, S., Zamora, M. L., Ying, Q., Lin, Y., Wang, W., Hu, M., and Wang,
708 Y.: Formation of urban fine particulate matter, *Chemical Reviews*, 115, 3803–3855,
709 10.1021/acs.chemrev.5b00067, 2015.

710 Zhang, W., Villarini, G., Vecchi, G. A., and Smith, J. A.: Urbanization exacerbated the rainfall
711 and flooding caused by hurricane Harvey in Houston, *Nature*, 563, 384+, 10.1038/s41586-018-
712 0676-z, 2018.

713 Zhao, B., Wang, Y., Gu, Y., Liou, K. N., Jiang, J. H., Fan, J., Liu, X., Huang, L., and Yung, Y.
714 L.: Ice nucleation by aerosols from anthropogenic pollution, 10.1038/s41561-019-0389-4, 2019.

715 Zhao, C. F., Lin, Y. L., Wu, F., Wang, Y., Li, Z. Q., Rosenfeld, D., and Wang, Y.: Enlarging
716 rainfall area of tropical cyclones by atmospheric aerosols, *Geophys. Res. Lett.*, 45, 8604–8611,
717 10.1029/2018gl079427, 2018.

718



719

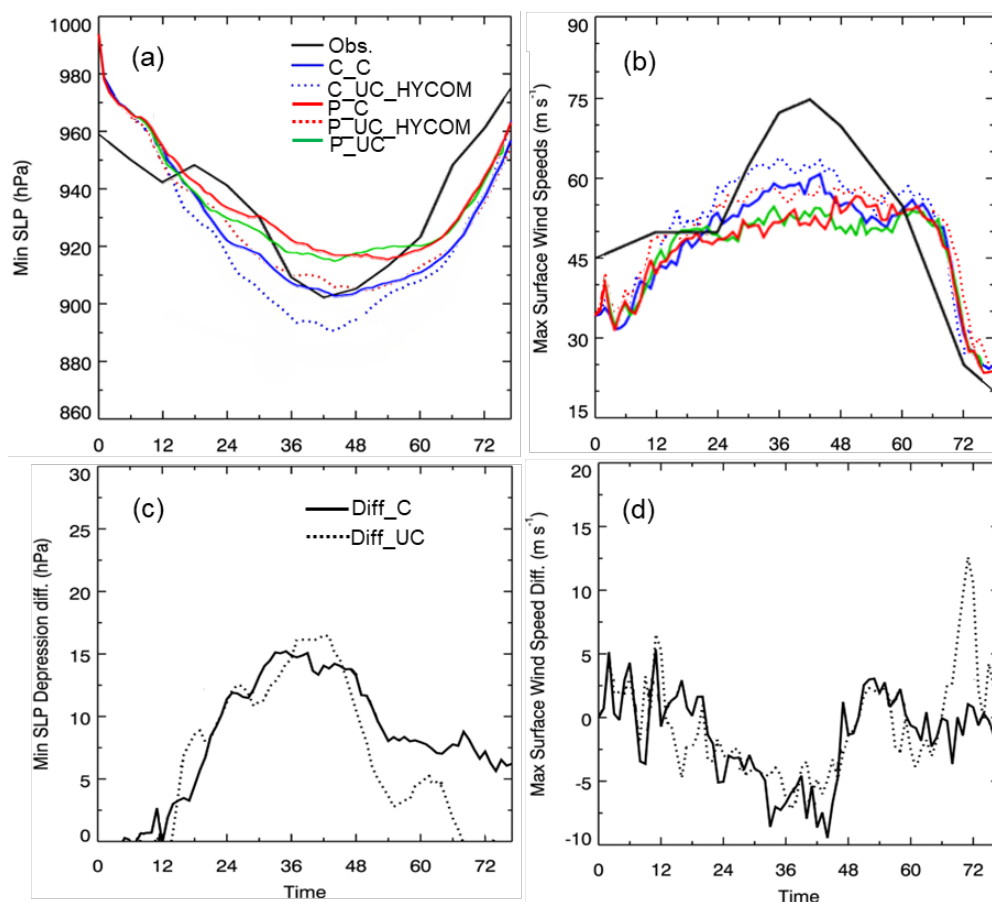
720 **Figure 1.** (a) MODIS AOD distribution averaged over the period prior to and during Hurricane

721 Katrina 2005 passage over the Gulf of Mexico (Aug. 24 – Aug. 31). (b) The initial condition of

722 aerosol concentrations with land-ocean contrast for the polluted case in CR-WRF. The black

723 square in (b) denotes the domain for the ROMS model.

724



725

726

727

728

729

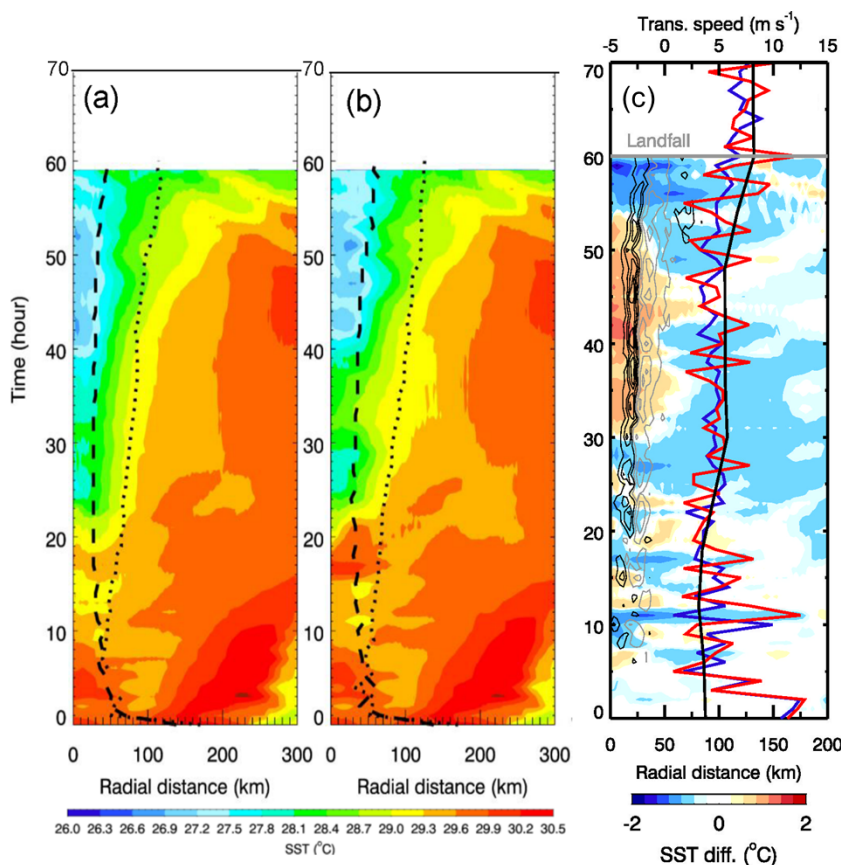
730

731

732

733

Figure 2. The simulated and observed evolution of the hurricane in terms of (a) minimum sea-level pressure (SLP) and (b) maximum surface (10-m) wind speed for the coupled and uncoupled simulations, i.e., C_C (blue solid lines) and P_C (red solid lines), C_UC_HYCOM (blue dotted lines) and P_UC_HYCOM (red dotted lines), as well as the P_UC case (solid green line). The differences of minimum SLP (c) and maximum surface (10-m) wind speed (d) between clean and polluted simulation are shown for the coupled (Diff_C = P_C – C_C, solid lines) and uncoupled cases (Diff_UC = P_UC_HYCOM – C_UC_HYCOM, dotted lines). The observations (black) in (a) and (b) are from the NHC Best Track Data.



734

735 **Figure 3.** Hovmöller diagrams of azimuthal mean SST fields for (a) C_C and (b) P_C, as well as

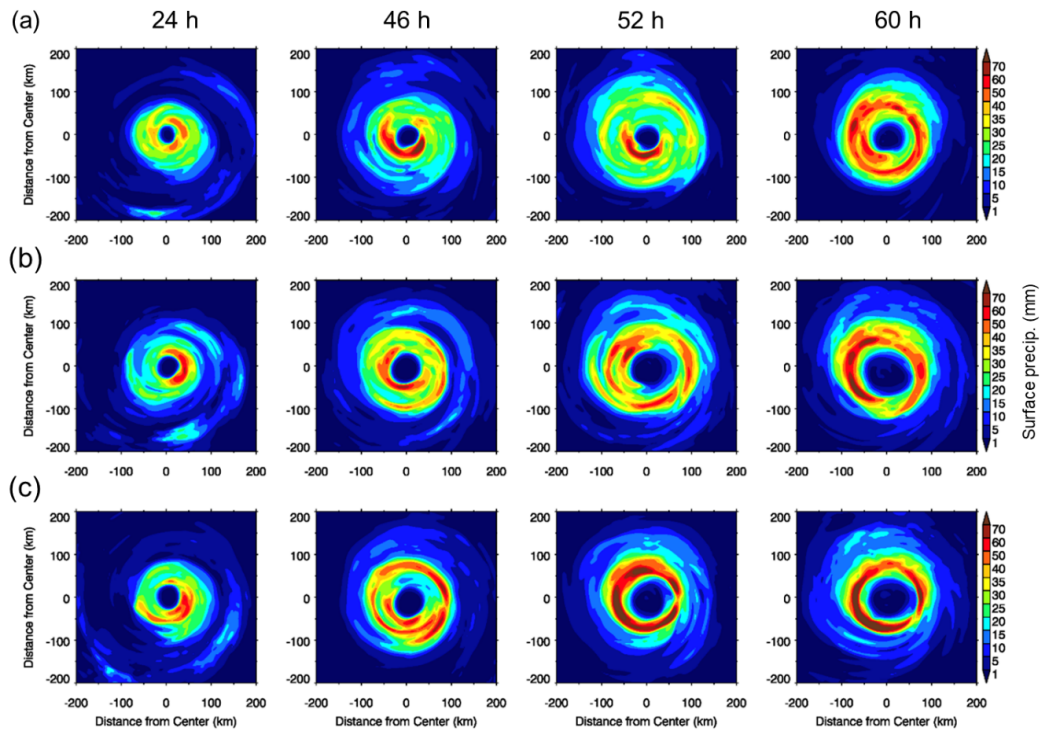
736 their differences (P_C - C_C). The solid and dash lines throughout the entire hurricane lifecycles

737 in panels (a-c) denote the RMW and the radii for the hurricane force wind (>34 m s⁻¹),

738 respectively. Contour lines in panel (c) denote the changes in surface wind stress curl (with an

739 interval of 0.25 N m⁻² and grey for positive and black for negative changes). The curves denote

740 the hurricane translation speeds for observation (black), C_C (blue), and P_C (red).



741

742 **Figure 4.** Horizontal distribution of precipitation rates for (a) C_C, (b) P_UC, and (c) P_C.

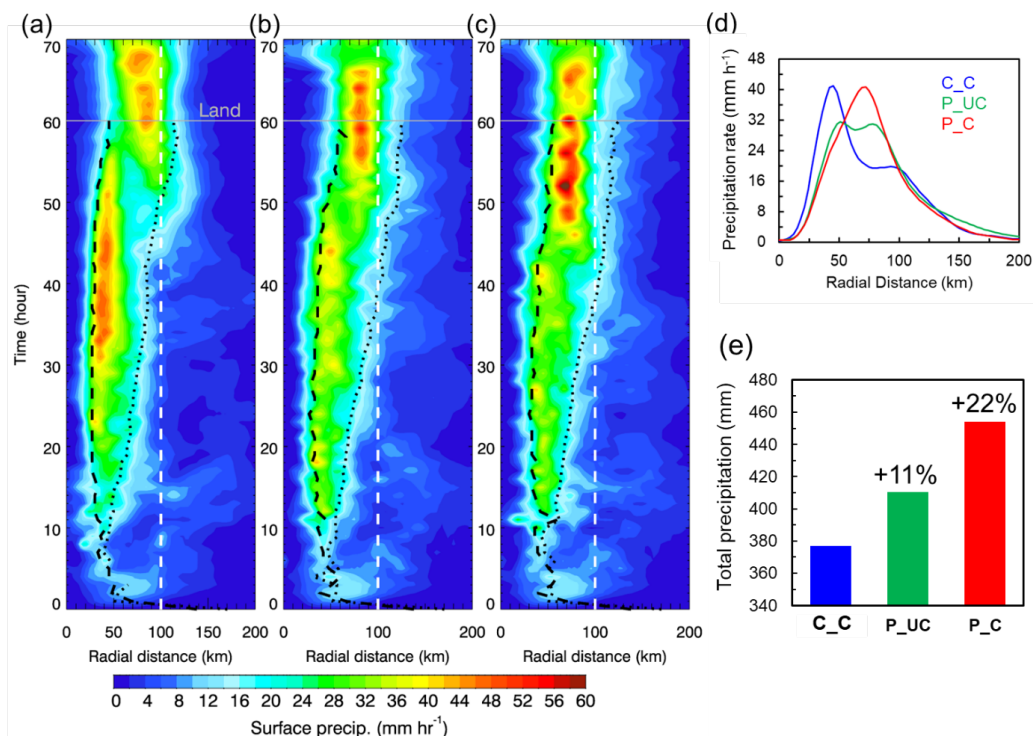
743 Snapshots at four times are displayed, including 24, 46, 52, and 60 h from the start of

744 simulations, corresponding to the developing stage, two mature stages, and dissipating stage of

745 TC, respectively.

746

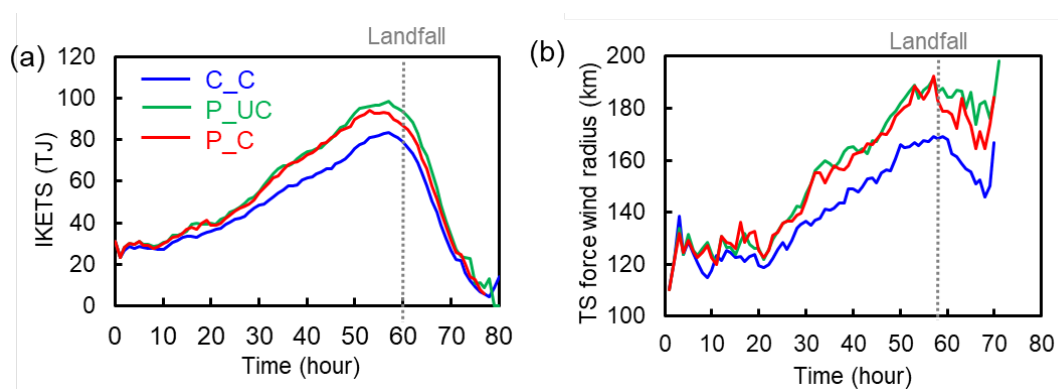
747



748

749 **Figure 5.** Hovmöller diagrams of the azimuthal means changes of precipitation rate for (a) C_C,
 750 (b) P_UC, and (c) P_C. The white dash lines in (a-c) denote the distance of 100 km away from
 751 the storm center. The solid and dash black lines (a-c) represent the radii of the maximum wind
 752 speed (RMW) and the hurricane force wind (with wind speed >32 m s⁻¹), respectively. (d)
 753 Azimuthally-averaged radial profiles of precipitation rate and (e) total accumulated precipitation
 754 for C_C (blue), P_UC (green), and P_C (red) within 100 km of the storm center during the
 755 mature stage of TC, corresponding to the time period of 40-55 h from the beginning of TC
 756 simulations.

757



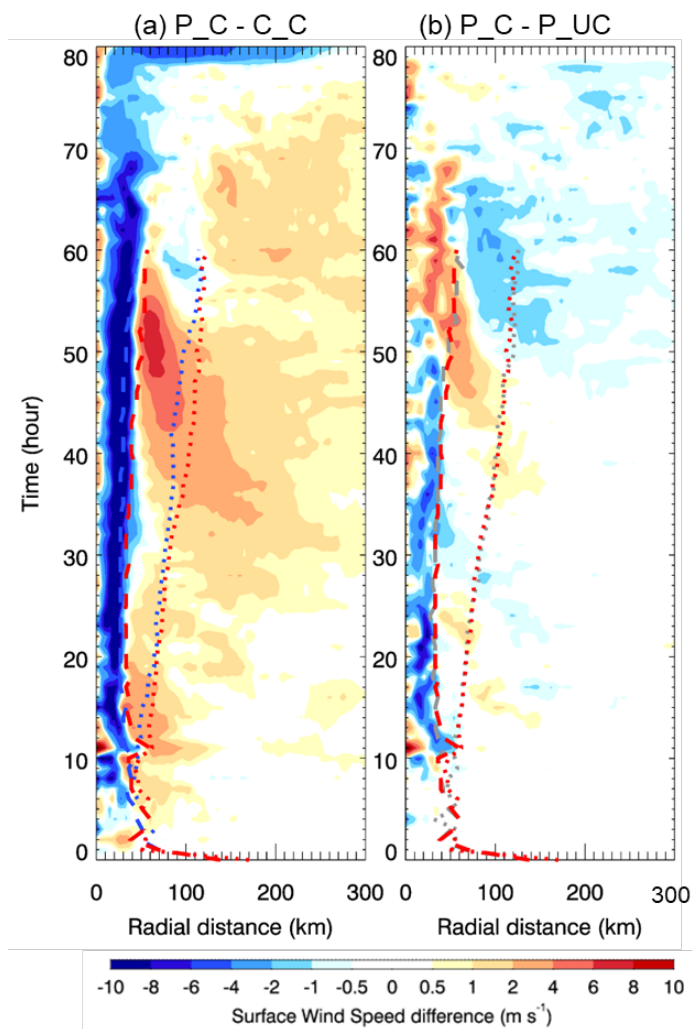
758

759 **Figure 6.** Temporal evolutions of (a) integrated kinetic energy (IKE) and (b) storm force radius

760 with winds higher than tropical storm force, i.e., 18 m s^{-1} , for C_C (blue), P_UC (green), and P_C

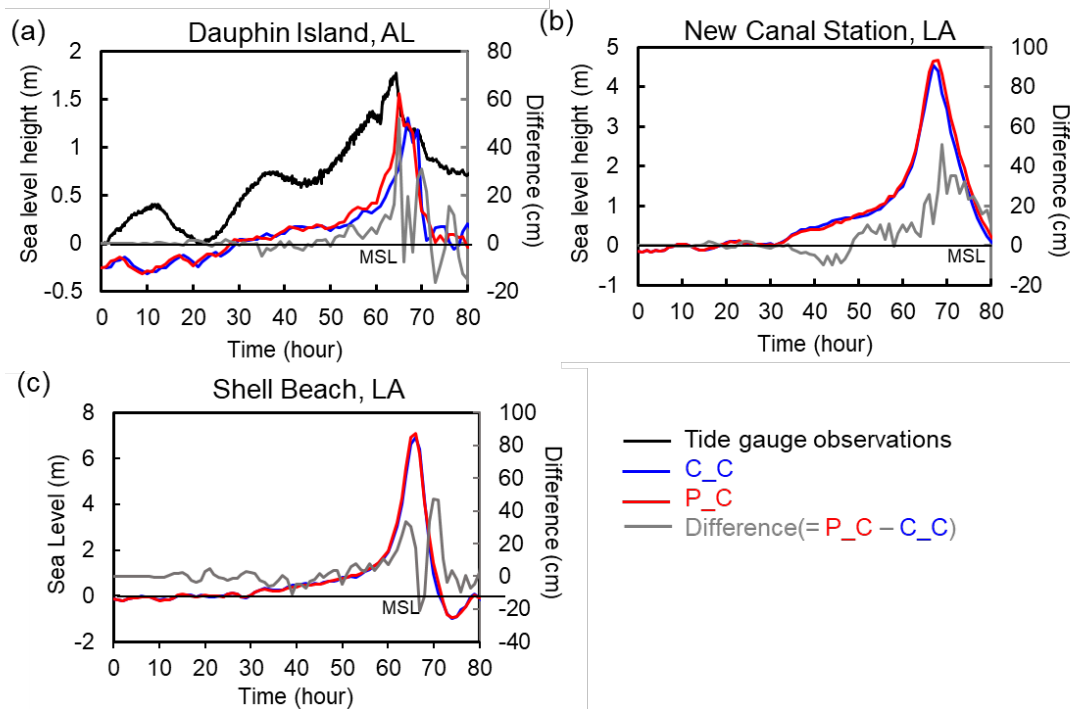
761 (red). The dot grey lines (a, b) denote the hurricane landfall time.

762



763

764 **Figure 7.** Hovmöller diagrams of the changes in azimuthal means of surface wind speed for (a)
765 P_C – C_C and (b) P_C – P_UC. The dashed and dotted curves throughout the entire hurricane
766 lifecycles denote the RMW and the radii for the hurricane force wind, respectively, with different
767 colors (blue, green, and red) representing different cases (C_C, P_UC, and P_C).



768

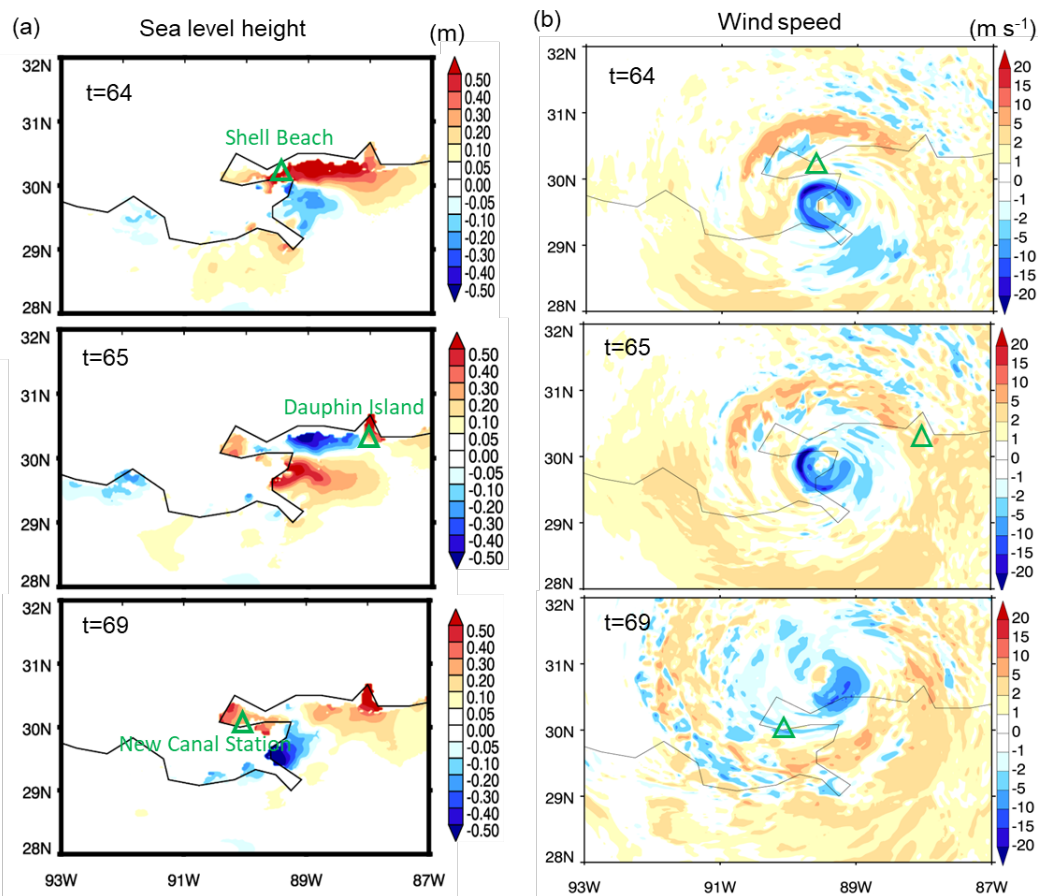
769 **Figure 8.** Sea level height at three coastal sites near New Orleans: (a) Dauphin Island, AL, (b)

770 New Canal Station, LA, and (c) Pass Christian, MS for C_C (blue) and P_C (red) cases. The

771 gauge observation (black line) is only available at Dauphin site in (a). The grey lines denote the

772 differences between P_C and C_C cases.

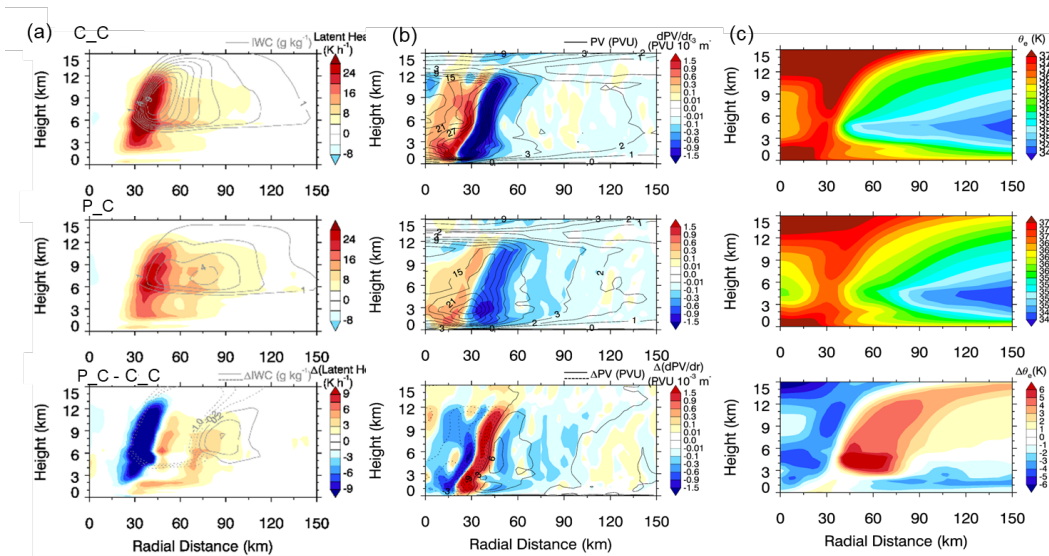
773



774

775 **Figure 9.** The differences (P_C – C-C) in (a) sea level height and (b) wind speed over New
776 Orleans coastal region at hour 64, 65, and 69 when Hurricane Katrina made landfall. The green
777 triangles in (a) denote the gauge station, including Shell Beach, AL, Dauphin Island, AL, and
778 New Canal Station, LA.

779



780

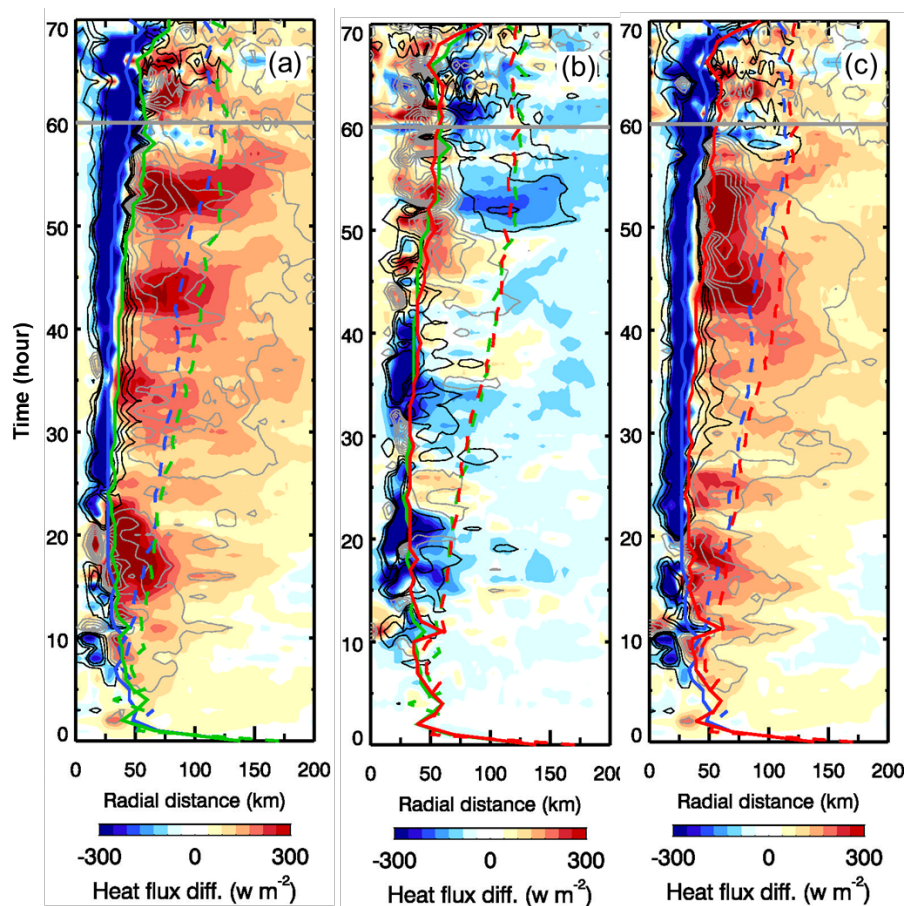
781 **Figure 10.** Vertical-radial cross-sections of 20-hr (32–52 hour) azimuthal means of (a) latent

782 heat overlaid with ice water content (IWC), (b) equivalent potential temperature (θ_e), and (c)

783 potential vorticity (PV) and its gradient for C_C, P_C case, and their difference (P_C - C_C)

784 from top to bottom.

785



786

787 **Figure 11.** Hovmöller diagrams of the changes of azimuthal means in surface wind stress

788 (contour lines, with an interval of 0.4 N m^{-2} and grey for positive and black for negative changes)

789 and surface total heat flux (color shading) induced by (a) aerosol only effect (i.e., $P_{UC} - C_C$),

790 (b) ocean coupling effect (i.e., $P_C - P_{UC}$), and (c) the combined effect (i.e., $P_C - C_C$). The

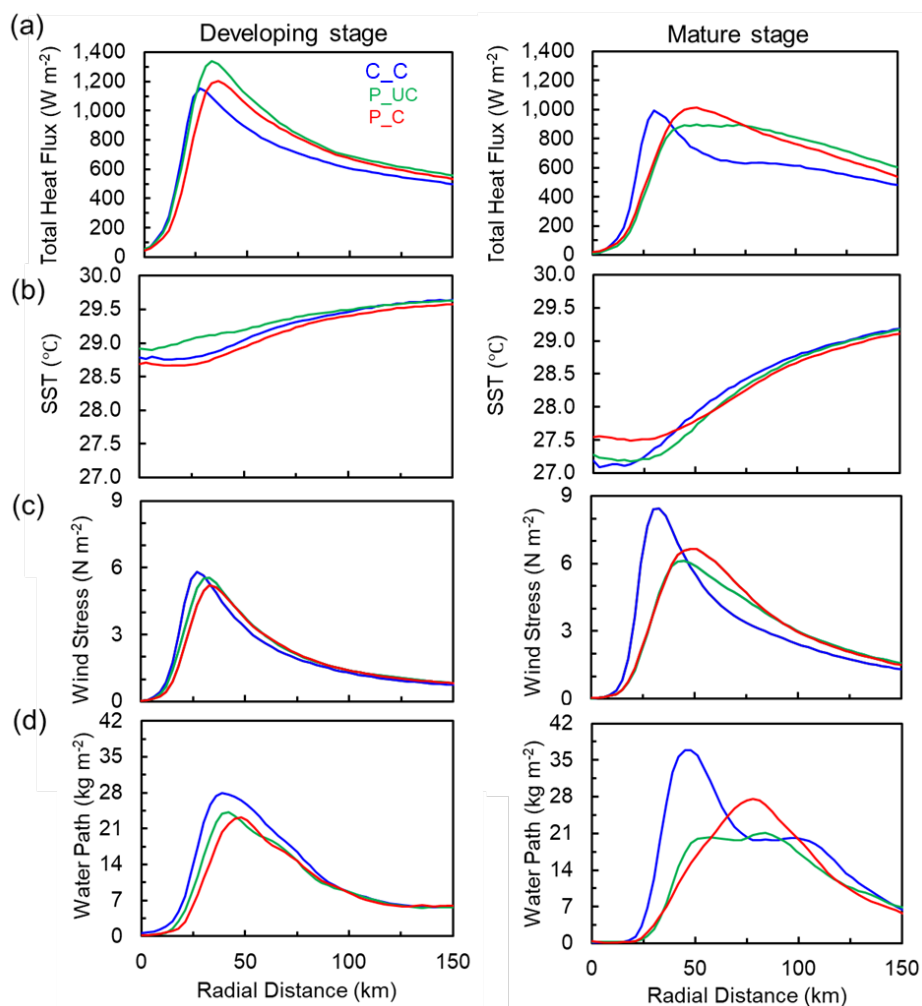
791 solid and dashed curves throughout the entire hurricane lifecycles denote the RMW and the radii

792 for the hurricane force wind ($>34 \text{ m s}^{-1}$), respectively, with different colors (blue, green, and red)

793 representing different cases (C_C , P_{UC} , and P_C). The positive (negative) perturbations denote

794 the upward (downward) flux, i.e., from the ocean (the atmosphere) to the atmosphere (the

795 ocean).

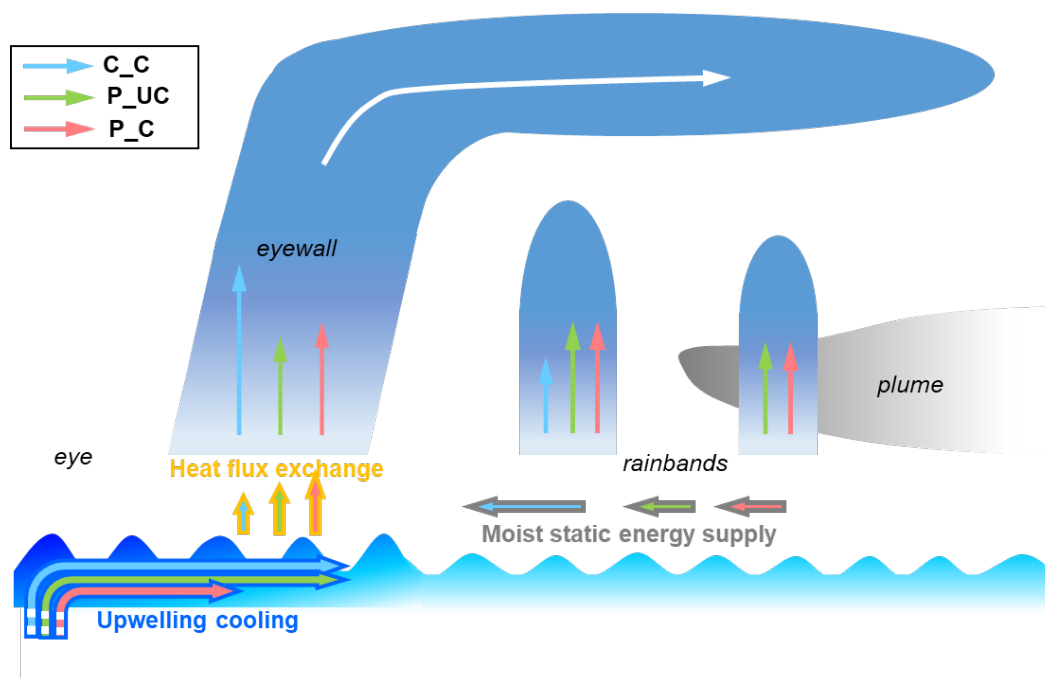


796

797 **Figure 12.** Azimuthally-averaged radial profiles for (a) total heat flux at the ocean surface, (b)
 798 SST, (c) wind stress, and (d) total condensate water path for C_C (blue), P_UC (green), and P_C
 799 (red) cases for the developing stage (15-28 h, left column) and mature stage (42-55 h, right
 800 column).

801

802



803

804 **Figure 13.** A schematic of the effects of anthropogenic aerosols and ocean feedback on a
 805 hurricane. The development of hurricane is characterized by convection in the outer rainbands
 806 and eyewall (vertical arrows). The moist static energy supply in the lower-level inflow (grey-
 807 edged horizontal arrows pointing from outer rainbands to storm core), the upwelling cooling in
 808 the ocean beneath the storm (blue-edged arrows starting in deep ocean and pointing from storm
 809 core to outer rainbands), and the heat flux exchange between the ocean and the storm (orange-
 810 edged vertical arrows pointing from the ocean to the storm near the storm core) are depicted in
 811 different types of arrows. The aerosol microphysical effect in the uncoupled polluted case
 812 (P_UC, green arrows) enhances convection in outer rainbands by invigorating mixed-phase
 813 cloud processes, leading to drier and colder lower-level inflow to the storm core and a weakened
 814 eyewall. Comparing the coupled polluted case (P_C, red arrows) to the coupled clean case (C_C,
 815 blue arrows), the weakening of the storm intensity by aerosols reduces the upwelling cooling in



816 the ocean because of the smaller surface wind stress. Consequently, the increased sea surface
817 temperature further re-energizes storm circulation. Therefore, the ocean coupling mitigates the
818 aerosol weakening effect to some extent. The overall effect of aerosol microphysical effects and
819 ocean coupling results in moderate enhancement of convection in the eyewall, stronger than that
820 in the clean case (blue arrows) but weaker than that in the uncoupled polluted case.



821 **Table 1. Experiment list.**

Cases	Aerosol configuration	Coupling	SST
C_C	The initial and boundary loadings of anthropogenic aerosols over land/ocean: 200/100 cm ⁻³ ; Sea salt: Initial concentration of 100 cm ⁻³ with continuous emissions as a function of surface wind speed	Yes	IC/BC based on HYCOM; Updated by ROMS every 10 min
C_UC_HY COM	As C_C	No	Constrained by HYCOM and fixed
P_C	As C_C, but with high loadings of anthropogenic aerosols over land/ocean of 1000/500 cm ⁻³	Yes	As C_C
P_UC	As P_C	No	Prescribed from outputs of C_C case
P_UC_HY COM	As P_C	No	Constrained by HYCOM and fixed

822